

Chiral Raman coupling for spin-orbit coupling in ultracold atomic gases

Biao Shan,¹ Lianghui Huang,^{1,*} Yuhang Zhao,¹ Guoqi Bian,¹ Pengjun Wang,¹ Wei Han,¹ and Jing Zhang^{1,2,†}

¹*State Key Laboratory of Quantum Optics Technologies and Devices,
Institute of Opto-electronics, Collaborative Innovation Center of Extreme Optics,
Shanxi University, Taiyuan, Shanxi 030006, China*

²*Hefei National Laboratory, Hefei, China.*

(Dated: February 11, 2025)

Spin-orbit coupling (SOC) in ultracold atoms is engineered by light-atom interaction, such as two-photon Raman transitions between two Zeeman spin states. In this work, we propose and experimentally realize chiral Raman coupling to generate SOC in ultracold atomic gases, which exhibits high quantization axis direction-dependence. Chiral Raman coupling for SOC is created by chiral light-atom interaction, in which a circularly polarized electromagnetic field generated by two Raman lasers interacts with two Zeeman spin states $\delta m_F = \pm 1$ (chiral transition). We present a simple scheme of chiral one-dimension (1D) Raman coupling by employing two Raman lasers at an intersecting angle 90° with the proper polarization configuration. In this case, Raman coupling for SOC exist in one direction of the magnetic quantization axis and disappears in the opposite direction. Then we extend this scheme into a chiral 2D optical square Raman lattice configuration to generate the 1D SOC. There are two orthogonal 1D SOC, which exists in the positive and negative directions of the magnetic quantization axis respectively. This case is compared with 2D SOC based on the nonchiral 2D optical Raman lattice scheme for studying the topological energy band. This work broadens the horizon for understanding chiral physics and simulating topological quantum systems.

I. INTRODUCTION

Chirality plays a critical role in a wide range of systems, from matter, light, and light-matter interaction [1, 2], which displays a kind of symmetry breaking characterized by lacking mirror-reflection symmetry [3] and has been attracting intense attention in a broad range of scientific areas. The recent discovery of exotic chiral matters and phenomena involving chiral superconductors [4], chiral skyrmions [5], chiral domain walls [6–8], chiral spintronics [9], chiral currents [10], chiral electrons [11], nanoscale chiral valley-photon interface [12], and chiral quantum optics [13], have aroused widespread interest. In particular, interaction between chiral light and chiral matter leads to chiral light-matter interaction, which triggers exiting research directions and new applications [14–16].

Recent experimental realization of spin-orbit coupling (SOC) in ultracold quantum gases by light-matter interaction [17–29] provides a highly controllable platform for the study of topological materials and exotic matter states [30–43]. In this paper, we explore chiral Raman coupling for SOC in ultracold atomic gases by chiral light-matter interaction, in which a circularly polarized electromagnetic field generated by two Raman lasers interacts with two Zeeman spin states $\delta m_F = \pm 1$. Chiral Raman coupling presents characteristics with high quantization axis direction-dependence. We employ two Raman lasers at an intersecting angle 90° with the proper polarization configuration to generate one-dimension (1D) SOC. Then we extend this case into a chiral 2D optical square Raman lattice to generate the SOC.

In Section 2, we introduce the chirality of spin motion in a static and AC magnetic field to better understand the physics of the chiral Raman coupling for SOC generated by chiral light-matter interaction. We then present a scheme of generating chiral 1D Raman coupling for SOC by employing two Raman lasers at an intersecting angle 90° with the proper polarization configuration in Section 3 and extend this case into a chiral 2D optical square Raman lattice in Section 4.

II. CHIRALITY OF SPIN MOTION IN A STATIC AND AC MAGNETIC FIELD

A spin-1/2 has a magnetic dipole moment μ_s . When subjected to an external magnetic field \mathbf{B} , a dipole moment experiences a torque \mathbf{L} according to $\mathbf{L} = \mu_s \times \mathbf{B}$ (known as Larmor precession). Magnetization is defined as the vector sum of the spin magnetic moments μ_s per unit volume, denoted by the symbol \mathbf{M}

$$\mathbf{M} = \frac{1}{V} \sum_{k=1}^N \mu_{sk} \quad (1)$$

The spin with angular momentum \mathbf{S} and magnetic moment μ_s is subjected to torque \mathbf{L} under the external magnetic field \mathbf{B} , which satisfies the equation

$$\frac{d\mathbf{S}}{dt} = \mathbf{L} = \mu_s \times \mathbf{B} \quad (2)$$

According to the formula $\mu_s = -\gamma\mathbf{S}$, Eq. (2) can be written as

$$\frac{d\mu_s}{dt} = -\gamma\mu_s \times \mathbf{B} \quad (3)$$

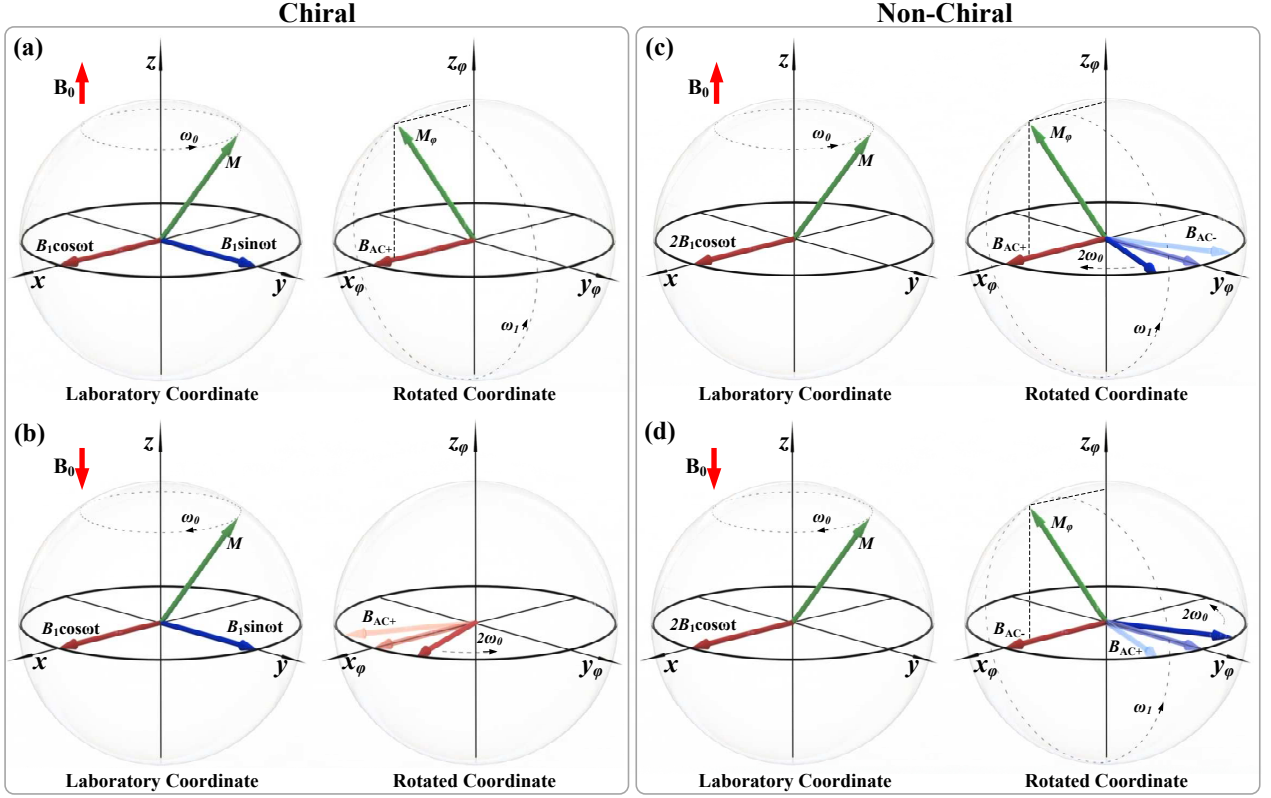


FIG. 1. (Color online). **Spin motion in a static and AC magnetic field.** (a) and (b) Spin motion for the circular polarization of AC magnetic field $\mathbf{B}_{AC+} = B_1 \cos \omega t \hat{\mathbf{e}}_x + B_1 \sin \omega t \hat{\mathbf{e}}_y$ with the strong, static magnetic field B_0 along the $+z$ (a) and $-z$ (b) respectively. When B_0 is along the $+z$ direction, the \mathbf{B}_{AC+} in the rotating coordinate leads to the magnetization \mathbf{M}_φ to rotate around x_φ at the frequency of ω_1 for $\omega = \omega_0$. When B_0 is along the $-z$ direction, the AC magnetic field \mathbf{B}_{AC+} will be the high-speed rotation at the frequency of $2\omega_0$ and its influence on the magnetization is negligible. This case is chiral since the chiral AC field induces the chiral interaction with spins. (c) and (d) Spin motion for the linear polarization of AC field $\mathbf{B}_{ACx} = 2B_1 \cos \omega t \hat{\mathbf{e}}_x$ with the strong, static magnetic field B_0 along the $+z$ (c) and $-z$ (d) respectively. When B_0 is along the $+z$ direction, only the component \mathbf{B}_{AC+} in the rotating coordinate leads to the magnetization \mathbf{M}_φ to rotate around x_φ at the frequency of ω_1 for $\omega = \omega_0$ and the component \mathbf{B}_{AC-} is neglected due to the high-speed rotation at the frequency of $2\omega_0$. When B_0 is reversed to the $-z$ direction, the role of two orthogonal circular components is reversed: the component \mathbf{B}_{AC-} leads to the magnetization \mathbf{M}_φ to rotate around x_φ and the component \mathbf{B}_{AC+} is neglected. Therefore, this case is non-chiral.

where γ is a proportionality constant called the gyromagnetic ratio. From the relation between \mathbf{M} and μ_s , the magnetization vector expression of Bloch equation can be obtained as

$$\frac{d\mathbf{M}}{dt} = -\gamma \mathbf{M} \times \mathbf{B} \quad (4)$$

Considering that a strong, static magnetic field B_0 along the z direction is used to align spins. When the spins initially are prepared along the z direction, an AC magnetic field \mathbf{B}_{AC} (Radio-frequency field) is applied, which is perpendicular to the z direction and then will rotate the spins away from B_0 called excitation. Note that the influence on the magnetization is negligible when AC magnetic field \mathbf{B}_{AC} is along the direction of B_0 . Here, AC magnetic field \mathbf{B}_{AC} has the polarization helicity $\sigma \in (-1, 1)$. The polarization helicity (the degree of circular polarization) is 0, ± 1 for linear, right- and left-hand circular polarization. Therefore, the chiral

AC magnetic field can induce the chiral interaction with atoms.

The chirality of spin motion in a static and AC magnetic field can be understood through the Bloch sphere in a laboratory and rotating coordinate systems as shown in Fig. 1. At the strong, static magnetic field B_0 along the $+z$ direction of the laboratory coordinate, the spins precess in the direction of the external magnetic field at the Larmor frequency $\omega_0 = \gamma B_0$. So the magnetization remains stationary when we consider transforming the laboratory coordinate system into a rotating coordinate system $(x_\varphi, y_\varphi, z_\varphi)$ that rotates around the z -axis at a frequency of ω_0 as shown in the right panels of Fig. 1. First, considering the circular polarization of AC magnetic field $\mathbf{B}_{AC+} = B_1 \cos \omega t \hat{\mathbf{e}}_x + B_1 \sin \omega t \hat{\mathbf{e}}_y$ with angular velocity ω as shown in Fig. 1(a), that is $\mathbf{B} = B_1 \cos \omega t \hat{\mathbf{e}}_x + B_1 \sin \omega t \hat{\mathbf{e}}_y + B_0 \hat{\mathbf{e}}_z$. So the Bloch equa-

tion can be written in laboratory coordinate

$$\begin{aligned}\frac{dM_x}{dt} &= \gamma(B_1M_z \sin \omega t - B_0M_y), \\ \frac{dM_y}{dt} &= \gamma(B_0M_x - B_1M_z \cos \omega t), \\ \frac{dM_z}{dt} &= \gamma(B_1M_y \cos \omega t - B_1M_x \sin \omega t).\end{aligned}\quad (5)$$

Bloch equation may be transformed into the rotating coordinate with the angular frequency ω with the transformation matrix shown as

$$\begin{pmatrix} \mathbf{M}_{\varphi x} \\ \mathbf{M}_{\varphi y} \\ \mathbf{M}_{\varphi z} \end{pmatrix} = \begin{pmatrix} \cos \omega t & \sin \omega t & 0 \\ -\sin \omega t & \cos \omega t & 0 \\ 0 & 0 & 1 \end{pmatrix} \begin{pmatrix} \mathbf{M}_x \\ \mathbf{M}_y \\ \mathbf{M}_z \end{pmatrix}\quad (6)$$

Therefore, Bloch equation in the rotating coordinate is given as

$$\begin{aligned}\frac{dM_{\varphi x}}{dt} &= -(\omega_0 - \omega)M_{\varphi y}, \\ \frac{dM_{\varphi y}}{dt} &= (\omega_0 - \omega)M_{\varphi x} - \omega_1M_{\varphi z}, \\ \frac{dM_{\varphi z}}{dt} &= \omega_1M_{\varphi y}.\end{aligned}\quad (7)$$

Here, $\omega_1 = \gamma B_1$. When choose $\omega = \omega_0$, the AC magnetic field \mathbf{B}_{AC+} always keeps along the x_φ direction in the rotating coordinate, then the magnetization \mathbf{M}_φ will rotate around x_φ at the frequency of ω_1 as shown in the right panel of Fig. 1(a). The frequency ω_1 that \mathbf{M}_φ rotates around B_{x_φ} is called the Rabi frequency. If B_0 is reversed to the $-z$ direction, the AC magnetic field B_{x_φ} will be the high-speed rotation at the frequency of $2\omega_0$ as shown in Fig. 1(b). Thus, the average time performance is close to zero, and the influence on the magnetization is negligible. This case is chiral since the chiral AC magnetic field induces the chiral interaction with spins.

Then considering the linear polarization of the AC magnetic field field $\mathbf{B}_{ACx} = 2B_1 \cos \omega t \hat{\mathbf{e}}_x$ applied in the x direction of the laboratory coordinate system as shown in Fig. 1(c). It can be decomposed into two orthogonal components $\mathbf{B}_{AC+} = B_1 \cos \omega t \hat{\mathbf{e}}_x + B_1 \sin \omega t \hat{\mathbf{e}}_y$ and $\mathbf{B}_{AC-} = B_1 \cos \omega t \hat{\mathbf{e}}_x - B_1 \sin \omega t \hat{\mathbf{e}}_y$ with the same amplitude, frequency and opposite directions of rotation. When the strong, static magnetic field B_0 is along the $+z$ direction, only the component \mathbf{B}_{AC+} in the rotating coordinate leads to the magnetization \mathbf{M}_φ to rotate around x_φ at the frequency of ω_1 for $\omega = \omega_0$ and the component \mathbf{B}_{AC-} is neglected due to the high-speed rotation at the frequency of $2\omega_0$. When B_0 is reversed to the $-z$ direction, the role of two orthogonal circular components is reversed: the component \mathbf{B}_{AC-} leads to the magnetization \mathbf{M}_φ to rotate around x_φ and the component \mathbf{B}_{AC+} is neglected as shown in Fig. 1(d). This case corresponds to non-chiral.

III. CHIRAL RAMAN COUPLING FOR SPIN-ORBIT COUPLING

As we all know, two Raman lasers can generate equivalently AC magnetic field \mathbf{B}_{AC} [33, 44, 45]. The effective magnetic field induced by the two Raman lasers $\mathbf{E} = \mathbf{E}_1 e^{-i\omega_L t} + \mathbf{E}_2 e^{-i(\omega_L + \delta\omega)t}$ can be wrote as

$$\mathbf{B}^{eff} = \frac{i\mu_v}{\mu_B g_J} \mathbf{E}^* \times \mathbf{E} = \mathbf{B}_{DC}^{eff} + \mathbf{B}_{AC}^{eff},\quad (8)$$

where

$$\mathbf{B}_{DC}^{eff} = \frac{i\mu_v}{\mu_B g_J} (\mathbf{E}_1^* \times \mathbf{E}_1 + \mathbf{E}_2^* \times \mathbf{E}_2),\quad (9)$$

$$\mathbf{B}_{AC}^{eff} = \frac{i\mu_v}{\mu_B g_J} (\mathbf{E}_1^* \times \mathbf{E}_2 e^{-i\delta\omega t} + \mathbf{E}_2^* \times \mathbf{E}_1 e^{i\delta\omega t}).\quad (10)$$

Here, ω_L is the frequency of the Raman lasers with the frequency difference $\delta\omega$, μ_v is the vector polarizability, μ_B is the Bohr magneton, g_J is the electronic spin Landé g-factor. From Eq. (9), we can see that the first term \mathbf{B}_{DC}^{eff} depends on the ellipticity of light, which corresponds to the effective DC magnetic field and is equivalent to the vector shift to generate linear Zeeman splitting (light shift proportional to m_F). The \mathbf{B}_{DC}^{eff} will add to the static bias field \mathbf{B}_{DC} to act on atoms. Therefore the influence on the magnetization is negligible when \mathbf{B}_{DC}^{eff} is perpendicular to the direction of B_0 . The second term \mathbf{B}_{AC}^{eff} corresponds to the effective AC magnetic field, in which only the components perpendicular to the direction of B_0 can drive Raman transitions between different energy levels $\delta m_F = \pm 1$. Here, $\delta m_F = \pm 1$ corresponds to the chiral transition. In this work, we only consider the second term \mathbf{B}_{AC}^{eff} and neglect the \mathbf{B}_{DC}^{eff} .

The Hamiltonian including light-atom interaction as the effective magnetic field interaction is given as

$$\begin{aligned}H &= \left[\frac{\hat{\mathbf{p}}^2}{2m} + V(\mathbf{r}) \right] \hat{I} + \frac{\hbar\omega_{hf}}{2} \hat{\sigma}_z \\ &+ \frac{\mu_B g_{m_{F'}}^{m_F}}{2} \mathbf{B}_0 \cdot \hat{\sigma} + \frac{\mu_B \eta_{m_{F'}}^{m_F}}{2} \mathbf{B}_{AC}^{eff} \cdot \hat{\sigma},\end{aligned}\quad (11)$$

where \hat{I} is the identity operator and $\hat{\sigma}$ is denoted with the three spin operators $(\hat{\sigma}_z, \hat{\sigma}_x, \hat{\sigma}_y)$ or $(\hat{\sigma}_z, \hat{\sigma}_+, \hat{\sigma}_-)$, $V(\mathbf{r})$ is trapping potential, and $\hat{\sigma}_\pm = (\hat{\sigma}_x \pm i\hat{\sigma}_y)/2$, $\eta_{m_{F'}}^{m_F}$ is a coupling constant. For some special geometry structure of the Raman lasers, the effective AC magnetic field \mathbf{B}_{AC}^{eff} is spatial dependent. As a result, one can realize spin-orbit coupling from the last term of Eq. (11).

A. Chiral 1D Raman coupling for spin-orbit coupling

Here, we employ two Raman lasers at an intersecting angle 90° in the x-y plane to generate chiral 1D

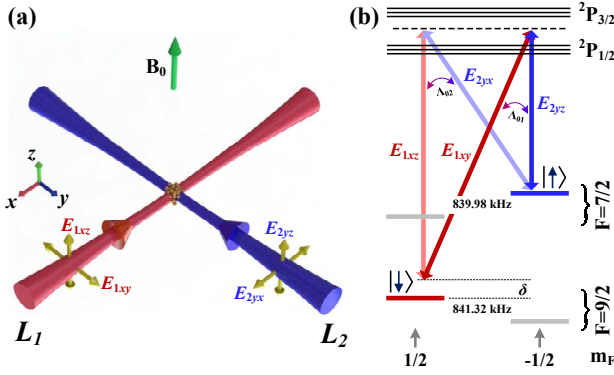


FIG. 2. (Color online). **Schematic of experimental scheme of 1D Raman coupling for SOC for $\delta m_F = \pm 1$ and the energy level of ^{40}K .** (a) The Raman lasers L_1 (red) and L_2 (blue) propagate along the x and y axis respectively. Here, the Raman coupling is induced by (E_{1xz}, E_{2yz}) and (E_{2yz}, E_{1xy}) . The external magnetic field B_0 along the z direction generates the Zeeman splitting and the quantization axis of the system. (b) Two hyperfine spin states are coupled with the electronic excited states through two Raman lasers L_1 and L_2 . Here, the Raman lasers drive the chiral transition $\delta m_F = \pm 1$ between $|F = 7/2, m_F = -1/2\rangle \equiv |\uparrow\rangle$ and $|F = 9/2, m_F = 1/2\rangle \equiv |\downarrow\rangle$.

Raman coupling for SOC. A homogeneous magnetic biased field $B_0=2.7$ G is applied in the z axis (gravity direction shown in Fig. 2), which defines the magnetic quantization axis and gives a Zeeman splitting. Two hyperfine Zeeman states $|F = 7/2, m_F = -1/2\rangle \equiv |\uparrow\rangle$ and $|F = 9/2, m_F = 1/2\rangle \equiv |\downarrow\rangle$ are chosen as the two spin states for Raman transition. The bichromatic light field of the Raman scheme is written as

$$\mathbf{E} = \mathbf{E}_{1\mathbf{x}} + \mathbf{E}_{2\mathbf{y}} \quad (12)$$

where

$$\begin{aligned} \mathbf{E}_{1\mathbf{x}} &= (\hat{\mathbf{e}}_z E_{1xz} + \hat{\mathbf{e}}_y E_{1xy} e^{i\varphi_1}) e^{-ik_R x} e^{-i(\omega_L + \delta\omega)t} \\ \mathbf{E}_{2\mathbf{y}} &= (\hat{\mathbf{e}}_z E_{2yz} + \hat{\mathbf{e}}_x E_{2yx} e^{i\varphi_2}) e^{-ik_R y} e^{-i\omega_L t} \end{aligned} \quad (13)$$

Here the φ_1 and φ_2 are the initial phase of two orthogonally polarized components of the laser beam 1 and 2 respectively, which determine the polarization helicity of the input Raman laser beam 1 and 2, as shown in Fig. 2(a). $k_R = 2\pi/\lambda$ is the wave number of the Raman laser with λ being the wavelength. The frequency difference $\delta\omega = \omega_{hf} + \mu_B g_{m_{F'}}^{m_F} B_0/\hbar + \delta$ differs by a small detuning δ from the hyperfine energy splitting ω_{hf} and the linear Zeeman shift between $\delta m_F = \pm 1$. Here, $g_{m_{F'}}^{m_F}$ depends on the hyperfine Landé g-factors g_F and $g_{F'}$.

Then, the effective AC magnetic field can be expressed as [33]

$$\mathbf{B}_{AC}^{eff} = \mathbf{B}_{AC-el}^{eff} e^{i\delta\omega t} e^{ik_R(x-y)} + \mathbf{B}_{AC-el}^{eff\dagger} e^{-i\delta\omega t} e^{-ik_R(x-y)} \quad (14)$$

where

$$\mathbf{B}_{AC-el}^{eff} = i\Lambda_{01} e^{-i\varphi_1} \hat{\mathbf{e}}_x + i\Lambda_{02} e^{i\varphi_2} \hat{\mathbf{e}}_y - i\Lambda_{03} e^{i(\varphi_2 - \varphi_1)} \hat{\mathbf{e}}_z. \quad (15)$$

Here,

$$\begin{aligned} \Lambda_{01} &= \frac{u_v}{\mu_B g_J} E_{1xy} E_{2yz}, \\ \Lambda_{02} &= \frac{u_v}{\mu_B g_J} E_{1xz} E_{2yx}, \\ \Lambda_{03} &= \frac{u_v}{\mu_B g_J} E_{1xy} E_{2yx}. \end{aligned} \quad (16)$$

Since the static bias field B_0 is along the z axis and Raman coupling drives transitions between different energy levels $\delta m_F = \pm 1$, the term $-i\Lambda_{03} e^{i(\varphi_2 - \varphi_1)} \hat{\mathbf{e}}_z$ of \mathbf{B}_{AC}^{eff} can be neglected. Here, \mathbf{B}_{AC-el}^{eff} and $\mathbf{B}_{AC-el}^{eff\dagger}$ represent the ellipticity of the effective AC magnetic field, which is determined by the phases φ_1 and φ_2 .

The time and space-dependence $e^{i[\delta\omega t + k_R(x-y)]}$ of \mathbf{B}_{AC}^{eff} can be eliminated via the unitary transformation $S = e^{i[\delta\omega t + k_R(x-y)]\hat{\sigma}_z/2}$ and the rotating wave approximation. The resulting Hamiltonian can be represented as

$$\begin{aligned} H_R &= \left[\frac{\hat{\mathbf{p}}^2}{2m} + V(r) \right] \hat{I} - \frac{\hbar k_R (p_x - p_y)}{2m} \hat{\sigma}_z \\ &\quad + \boldsymbol{\Omega} \cdot \hat{\sigma} + \frac{(\hbar k_R)^2}{4m} \end{aligned} \quad (17)$$

where

$$\begin{aligned} \boldsymbol{\Omega} \cdot \hat{\sigma} &= \Omega_z \hat{\sigma}_z + \Omega \hat{\sigma}_- + \Omega^\dagger \hat{\sigma}_+, \\ \Omega_z &= -\frac{\hbar\delta}{2}, \\ \Omega &= \frac{\mu_B \eta_{m_{F'}}^{m_F}}{2} \mathbf{B}_{AC-el}^{eff} \cdot (\hat{\mathbf{e}}_x + i\hat{\mathbf{e}}_y), \\ \Omega^\dagger &= \frac{\mu_B \eta_{m_{F'}}^{m_F}}{2} \mathbf{B}_{AC-el}^{eff\dagger} \cdot (\hat{\mathbf{e}}_x - i\hat{\mathbf{e}}_y). \end{aligned} \quad (18)$$

Then we can obtain the simplified Hamiltonian as

$$\begin{aligned} H_R &= \left[\frac{\hat{\mathbf{p}}^2}{2m} + V(r) \right] \hat{I} - \frac{\hbar k_R (p_x - p_y)}{2m} \hat{\sigma}_z - \frac{\hbar\delta}{2} \hat{\sigma}_z \\ &\quad + \frac{\mu_B \eta_{m_{F'}}^{m_F}}{2} \Lambda_{01} [\sin \varphi_1 \sigma_x + \cos \varphi_1 \sigma_y] \\ &\quad - \frac{\mu_B \eta_{m_{F'}}^{m_F}}{2} \Lambda_{02} [\cos \varphi_2 \sigma_x + \sin \varphi_2 \sigma_y]. \end{aligned} \quad (19)$$

When B_0 is reversed to the $-z$ direction, the role of two orthogonal circular components of the effective AC magnetic field is reversed

$$\begin{aligned} \Omega &= \frac{\mu_B \eta_{m_{F'}}^{m_F}}{2} \mathbf{B}_{AC-el}^{eff\dagger} \cdot (\hat{\mathbf{e}}_x + i\hat{\mathbf{e}}_y), \\ \Omega^\dagger &= \frac{\mu_B \eta_{m_{F'}}^{m_F}}{2} \mathbf{B}_{AC-el}^{eff} \cdot (\hat{\mathbf{e}}_x - i\hat{\mathbf{e}}_y). \end{aligned} \quad (20)$$

The Hamiltonian in Eq. (28) describes a 1D SOC consisting of equal sum of Rashba and Dresselhaus terms.

This system is non-trivial due to the non-commutativity between the Abelian gauge potential $\mathcal{A} = \hbar k_R(\hat{\mathbf{e}}_x - \hat{\mathbf{e}}_y)/2$ and an additional Raman coupling term $\mathbf{\Omega} \cdot \hat{\sigma}$, and leads to lots of interesting phenomena studied both theoretically [40, 46–49] and experimentally [31, 35–39, 42].

To simplify without losing generality, we choose $|E_{1xy}| = |E_{1xz}| = |E_{2yz}| = |E_{2yx}|$ ($\Lambda_{01} = \Lambda_{02} = \Omega_0/\mu_B\eta_{m_F}^{m_F}$). For the setting with $(\varphi_1, \varphi_2) = (-\pi/2, 0)$ shown in Fig. 3(a1), $\mathbf{\Omega} = \Omega^\dagger = \Omega_0$ and $\mathbf{\Omega} \cdot \hat{\sigma} = -\hat{\sigma}_z\delta/2 - \Omega_0\hat{\sigma}_x$. This corresponds to generate the effective circular polarization (see Eq. (15)) of the AC magnetic field and leads to the Raman coupling term $-\Omega_0\hat{\sigma}_x$. When B_0 is reversed to the $-z$ direction (Fig. 3(b1)), this is similar to the setting with $(\varphi_1, \varphi_2) = (\pi/2, 0)$ to generate the orthogonal effective circular polarization of the AC magnetic field. Then we have $\mathbf{\Omega} \cdot \hat{\sigma} = -\hat{\sigma}_z\delta/2$, which means that the Raman coupling disappears. Therefore this case corresponds to chiral 1D Raman coupling for SOC since the effective chiral RF field induces the chiral interaction with atoms.

For the setting with $(\varphi_1, \varphi_2) = (0, 0)$ shown in Fig. 3(c1), $\mathbf{\Omega} = -\Omega_0(1 - i)/2$, $\mathbf{\Omega}^\dagger = -\Omega_0(1 + i)/2$ and $\mathbf{\Omega} \cdot \hat{\sigma} = -\hat{\sigma}_z\delta/2 - \Omega_0(\hat{\sigma}_x - \hat{\sigma}_y)/2$. This corresponds to generate the effective linear polarization of the RF field and leads to the Raman coupling term $-\Omega_0(\hat{\sigma}_x - \hat{\sigma}_y)/2$. When B_0 is reversed to the $-z$ direction shown in Fig. 3(d1), $\mathbf{\Omega} = \Omega_0(1 - i)/2$, $\mathbf{\Omega}^\dagger = \Omega_0(1 + i)/2$ and $\mathbf{\Omega} \cdot \hat{\sigma} = -\hat{\sigma}_z\delta/2 + \Omega_0(\hat{\sigma}_x - \hat{\sigma}_y)/2$. Therefore this case corresponds to non-chiral 1D Raman coupling for SOC since the similar SOC exists in $\pm z$ directions of the magnetic quantization axis.

Furthermore, we consider the special case of driving Raman transition between different energy levels with $\delta m_F = 0$, which corresponds to the nonchiral transition, such as two hyperfine Zeeman states $|F = 7/2, m_F = 1/2\rangle \equiv |\uparrow\rangle$ and $|F = 9/2, m_F = 1/2\rangle \equiv |\downarrow\rangle$. Only the component $\Lambda_{03}e^{-i(\varphi_2 - \varphi_1)}\hat{\mathbf{e}}_z$ of the effective AC magnetic field \mathbf{B}_{AC}^{eff} (Eq. (15)) parallel to the static bias field \mathbf{B}_0 can drive transition $\delta m_F = 0$ and the components of $\Lambda_{01}e^{-i\varphi_1}\hat{\mathbf{e}}_x$ and $\Lambda_{02}e^{i\varphi_2}\hat{\mathbf{e}}_y$ perpendicular to the static bias field \mathbf{B}_0 are neglected. Therefore, $\mathbf{\Omega}$ and $\mathbf{\Omega}^\dagger$ in Eq. (29) are expressed as

$$\begin{aligned}\mathbf{\Omega} &= \frac{\mu_B\eta_{m_F}^{m_F}}{2}\mathbf{B}_{AC-el}^{eff} \cdot \hat{\mathbf{e}}_z, \\ \mathbf{\Omega}^\dagger &= \frac{\mu_B\eta_{m_F}^{m_F}}{2}\mathbf{B}_{AC-el}^{eff\dagger} \cdot \hat{\mathbf{e}}_z.\end{aligned}\quad (21)$$

Here, the amplitudes of $\mathbf{\Omega}$ and $\mathbf{\Omega}^\dagger$ are independent of the relative phase (φ_1, φ_2) . When B_0 is reversed to the $-z$ direction, $\mathbf{\Omega}$ and $\mathbf{\Omega}^\dagger$ remain unchanged according to Eq. (21). Therefore this case corresponds to non-chiral 1D Raman coupling for SOC since the similar SOC exists in $\pm z$ directions of the magnetic quantization axis. It should be noted that the non-chiral Raman coupling with $\delta m_F = 0$ can be experimentally observed both in

1D and 2D. For simplicity, we only present the observation for 2D in the following, which is sufficient and more representative for verifying the theoretical analysis.

The experimental setup of ^{87}Rb and ^{40}K Bose-Fermi mixture is presented in detail with our previous works [50–52]. The experiment starts with the preparation of a degenerate Fermi gas of ^{40}K atoms in the state $|F = 9/2, m_F = 9/2\rangle$ in a crossed optical dipole trap. Around $N = 3 \times 10^6$ ultracold ^{40}K atoms are prepared at a temperature of $0.3T_F$ using sympathetic cooling by ^{87}Rb , where the Fermi temperature is defined by $T_F = \hbar\bar{\omega}(6N)^{1/3}/k_B$. Here $\bar{\omega} = (\omega_x\omega_y\omega_z)^{1/3} \simeq 2\pi \times 80$ Hz is the geometric mean of the optical trap in our experiment, N is the particle number of ^{40}K atoms, and k_B is the Boltzmann's constant. The remaining ^{87}Rb atoms are optically removed by applying a resonant laser beam pulse (780 nm) for 0.03 ms without heating and losing ^{40}K atoms. The initial spin state $|F = 9/2, m_F = 1/2\rangle \equiv |\downarrow\rangle$ is prepared in a rapid adiabatic passage induced by sweeping a Radio frequency (RF) field from $|F = 9/2, m_F = 9/2\rangle$ in 50 ms.

A pair of Raman lasers is located at the tune-out wavelength $\lambda = 768.98$ nm [53], which is extracted from a CW Ti-sapphire single-frequency laser. Therefore, the Raman laser approaches zero AC-stark energy shift for free atoms [54]. The recoil energy $E_R = (\hbar k_R)^2/2m = h \times 8.44$ kHz is taken as the natural energy units. The Raman laser beam L_1 is frequency-shifted around $+380.808$ MHz by a single-pass acousto-optic modulator (AOM), and L_2 is frequency-shifted -226.25×4 MHz through two AOMs in double-pass configuration respectively, which match the hyperfine transition frequency $\omega_{hf} = 1.28$ GHz.

Here, we employ the momentum-resolved Raman spectroscopy of an ultracold Fermi gas to check the chiral Raman coupling for SOC. We apply a Raman laser pulse with the duration time of $35 \mu\text{s}$ and measure the spin population for different frequency differences $\delta\omega$ of the Raman lasers. After the Raman pulse, we immediately turn off the optical trap and the homogeneous magnetic field, let the atoms free expand in 12 ms and take the time-of-flight (TOF) absorption image. The absorption images of two different hyperfine states for different frequency differences $\delta\omega$ of the Raman lasers are shown in Fig. 3. We can see that only atoms in certain momentum state are transferred from $|F = 9/2, m_F = 1/2\rangle \equiv |\downarrow\rangle$ to $|F = 7/2, m_F = -1/2\rangle \equiv |\uparrow\rangle$, which is determined by the frequency difference of the Raman lasers shown in Fig. 3. It shows the momentum-resolved features of Raman spectroscopy.

Consider that the polarization of the Raman laser L_1 along x is chosen as circular while L_2 along y as linear at a $\pi/4$ angle to the vertical direction as shown in Fig. 3(a1). This case corresponds to $|E_{1xy}| = |E_{1xz}| = |E_{2yz}| = |E_{2yx}|$ and the setting with $(\varphi_1, \varphi_2) = (-\pi/2, 0)$ to generate the effective circular polarization of RF field. The absorption images for the momentum-resolved Ra-

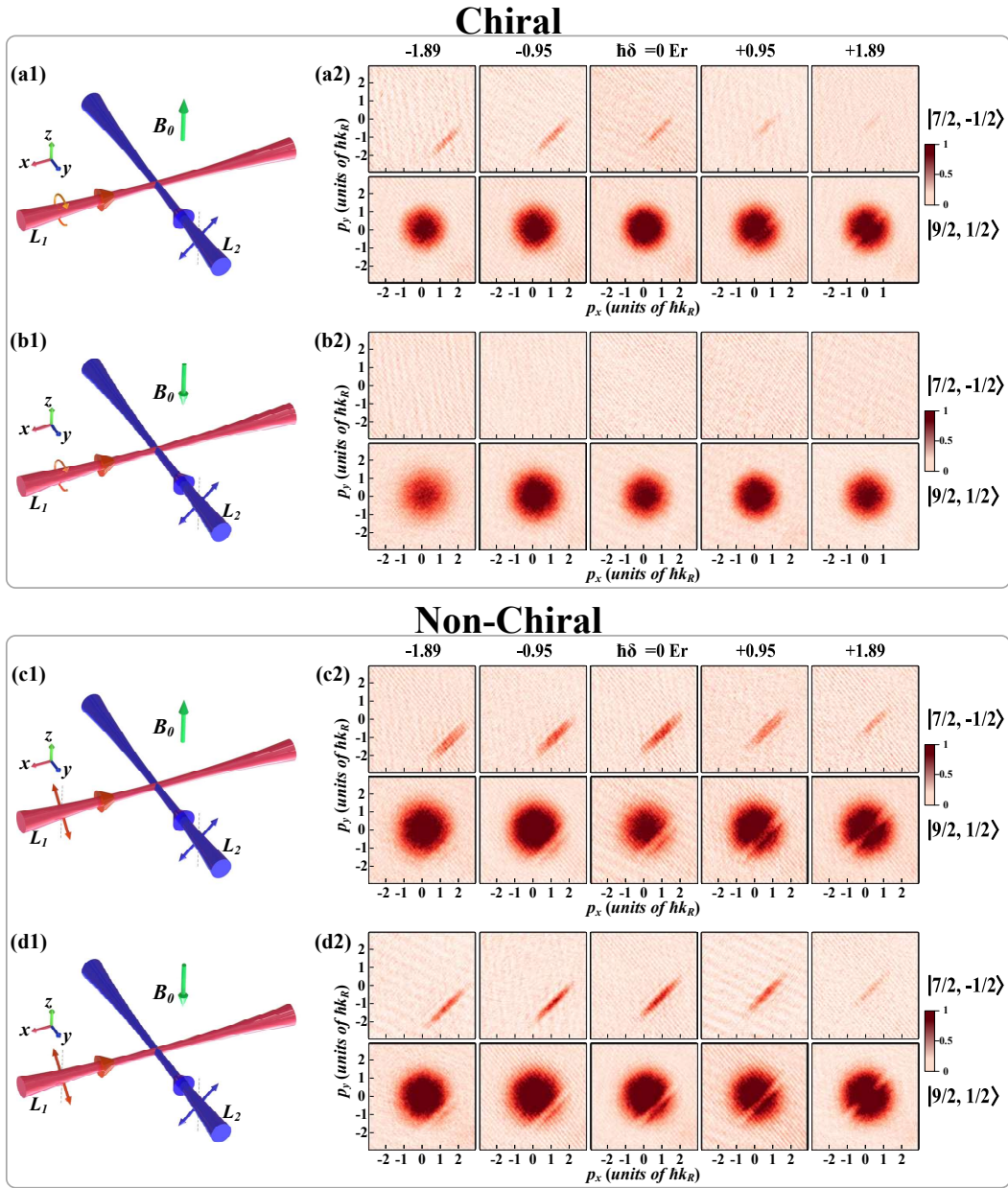


FIG. 3. (Color online). **Raman spectroscopy of 1D Raman coupling for SOC for $\delta m_F = \pm 1$.** (a) and (b) Chiral 1D Raman coupling for SOC. The external magnetic field B_0 is along the $+z$ direction for (a) and $-z$ direction for (b), respectively. (a1) and (b1) The polarization of the Raman laser L_1 along x is circular while L_2 along y is linear at a $\pi/4$ angle to the vertical direction. (a2) and (b2) The absorption images of two hyperfine spin states after 12 ms TOF for the different Raman two-photon-detuning δ . (c) and (d) Nonchiral 1D Raman coupling for SOC. (c1) and (d1) The polarization of the Raman laser L_1 and L_2 is linear and orthogonal at the $\pm\pi/4$ angle to the vertical direction. (c2) and (d2) The absorption images of two hyperfine spin states after 12 ms TOF for the different Raman two-photon detuning δ .

man spectroscopy in Fig. 3(a2) demonstrate the existence of the Raman coupling $\Omega_0 \hat{\sigma}_x$. In contrast, when B_0 is reversed to the $-z$ direction as shown in Fig. 3(b1) (or the polarization of L_1 is changed into the orthogonal circular state) which corresponds to the setting with $(\varphi_1, \varphi_2) = (\pi/2, 0)$ to generate the orthogonal effective circular polarization of AC magnetic field, there is no Raman coupling as shown in Fig. 3(b2). Therefore the

chiral 1D Raman coupling for SOC is realized experimentally by the chiral interaction between the effective AC magnetic field and atoms.

Consider that the polarization of the Raman laser L_1 and L_2 is linear and orthogonal at the $\pm\pi/4$ angle to the vertical direction respectively as shown in Fig. 3(c1) and (d1). This case corresponds to the setting with $(\varphi_1, \varphi_2) = (0, 0)$ to generate the effective linear po-

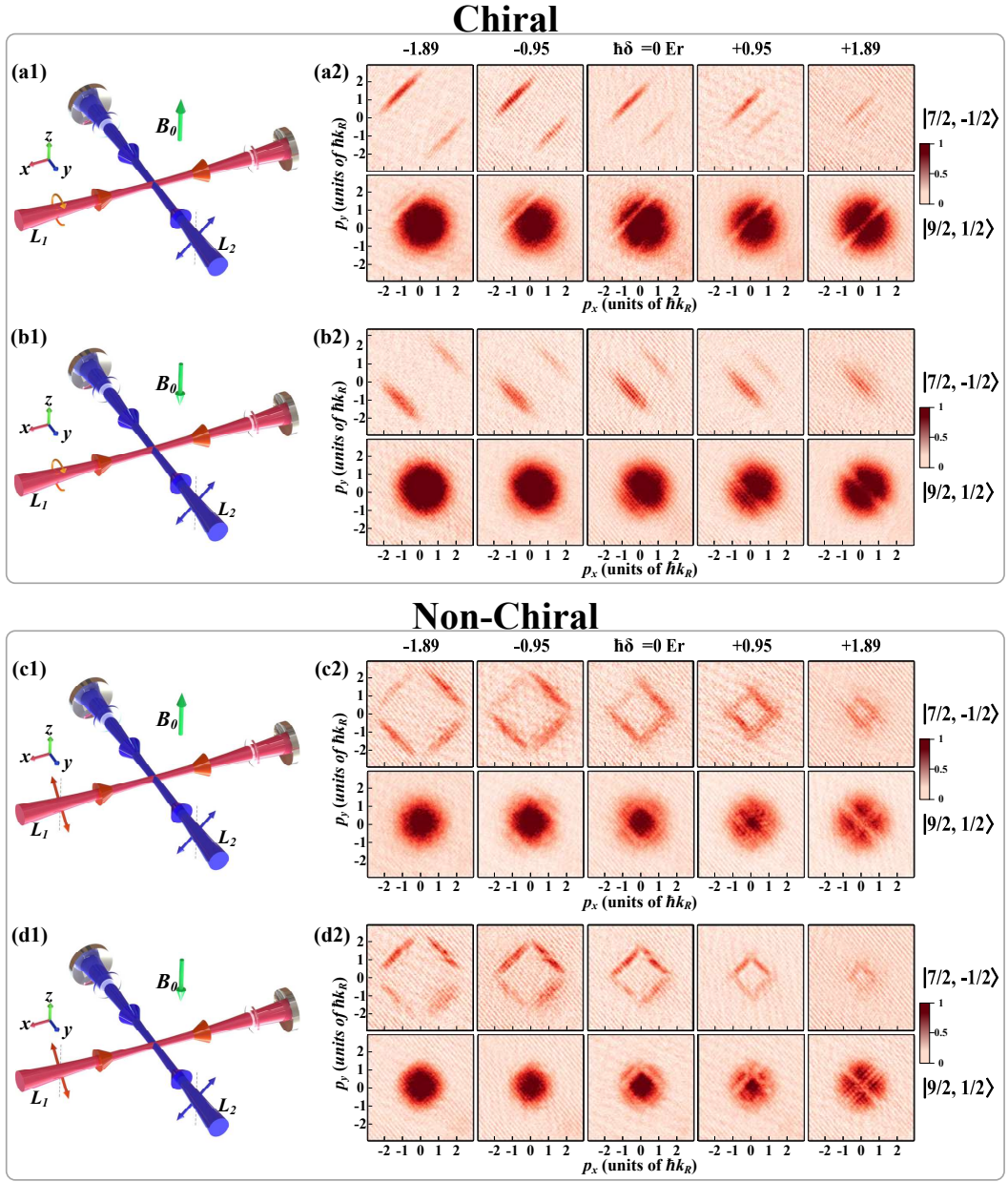


FIG. 4. (Color online). **Raman spectroscopy of 2D Raman coupling for SOC in an optical square Raman lattice for $\delta m_F = \pm 1$.** (a) and (b) 2D chiral Raman coupling for SOC. The external magnetic field B_0 is along the $+z$ direction for (a) and $-z$ direction for (b), respectively. (a1) and (b1) The polarization of the Raman laser L_1 along x is circular while L_2 along y is linear at a $\pi/4$ angle to the vertical direction. (a2) and (b2) The absorption images of two hyperfine spin states after 12 ms TOF for the different Raman two-photon detuning δ . (c) and (d) 2D nonchiral Raman coupling for SOC. (c1) and (d1) The polarization of the Raman laser L_1 and L_2 is linear and orthogonal at the $\pm\pi/4$ angle to the vertical direction. (c2) and (d2) The absorption images of two hyperfine spin states after 12 ms TOF for the different Raman two-photon detuning δ .

larization of the AC magnetic field. We can see that there always are Raman coupling in $\pm z$ directions of the magnetic quantization axis from the absorption images for the momentum-resolved Raman spectroscopy in Fig. 3(c2) and (d2). Therefore this case corresponds to non-chiral 1D Raman coupling for SOC.

B. Chiral 2D Raman coupling for SOC in an optical square Raman lattice

The two Raman lasers \mathbf{E}_{1x} and \mathbf{E}_{2y} are incident from x and y directions respectively and retro-reflected by two mirrors. The bichromatic light field of the Raman lattice

scheme is written as

$$\mathbf{E} = \mathbf{E}_{1\mathbf{x}} + \mathbf{E}_{2\mathbf{y}}, \quad (22)$$

where

$$\begin{aligned} \mathbf{E}_{1\mathbf{x}} &= 2[\hat{\mathbf{e}}_z E_{1xz} \cos(k_R x) \\ &\quad + \hat{\mathbf{e}}_y E_{1xy} e^{i\varphi_1} e^{i\frac{\alpha}{2}} \cos\left(k_R x + \frac{\alpha}{2}\right)] e^{-i(\omega_L + \delta\omega)t}, \\ \mathbf{E}_{2\mathbf{y}} &= 2[\hat{\mathbf{e}}_z E_{2yz} \cos(k_0 y) \\ &\quad + \hat{\mathbf{e}}_x E_{2yx} e^{i\varphi_2} e^{i\frac{\beta}{2}} \cos\left(k_R y + \frac{\beta}{2}\right)] e^{-i\omega_L t}. \end{aligned} \quad (23)$$

Here, α (β) is the extra relative phase difference between two orthogonal polarization components acquired by E_{1xy} (E_{2yx}) via a wave plate before and after the retro-reflected mirror.

Then, the effective AC magnetic field can be expressed as

$$\mathbf{B}_{AC}^{\text{eff}} = \mathbf{B}_{AC-el}^{\text{eff}} e^{i\delta\omega t} + \mathbf{B}_{AC-el}^{\text{eff}\dagger} e^{-i\delta\omega t} \quad (24)$$

where

$$\begin{aligned} \mathbf{B}_{AC-el}^{\text{eff}} &= iM_x e^{-i(\varphi_1 + \alpha/2)} \hat{\mathbf{e}}_x + iM_y e^{i(\varphi_2 + \beta/2)} \hat{\mathbf{e}}_y \\ &\quad - iM_z e^{i(\varphi_2 - \varphi_1 + \beta/2 - \alpha/2)} \hat{\mathbf{e}}_z \end{aligned} \quad (25)$$

Here,

$$\begin{aligned} M_x &= \Lambda_{01} \cos(k_R x + \alpha/2) \cos(k_0 y), \\ M_y &= \Lambda_{02} \cos(k_R y + \beta/2) \cos(k_0 x), \\ M_z &= \Lambda_{03} \cos(k_R x + \alpha/2) \cos(k_R y + \beta/2). \end{aligned} \quad (26)$$

and

$$\begin{aligned} \Lambda_{01} &= 4 \frac{u_v}{\mu_B g J} E_{1xy} E_{2yz}, \\ \Lambda_{02} &= 4 \frac{u_v}{\mu_B g J} E_{2yx} E_{1xz}, \\ \Lambda_{03} &= 4 \frac{u_v}{\mu_B g J} E_{1xy} E_{2yx}. \end{aligned} \quad (27)$$

The time-dependence $e^{i\delta\omega t}$ of $\mathbf{B}_{AC}^{\text{eff}}$ can be eliminated via the unitary transformation $S = e^{i\delta\omega t \hat{\sigma}_z / 2}$ and the rotating wave approximation. The resulting Hamiltonian can be represented as

$$H_R = \left[\frac{\hat{\mathbf{p}}^2}{2m} + V(r) \right] \hat{I} + \mathbf{\Omega} \cdot \hat{\sigma} \quad (28)$$

where

$$\begin{aligned} \mathbf{\Omega} \cdot \hat{\sigma} &= \Omega_z \hat{\sigma}_z + \Omega \hat{\sigma}_- + \Omega^\dagger \hat{\sigma}_+, \\ \Omega_z &= -\frac{\hbar\delta}{2}, \\ \Omega &= \bar{M}_x [\sin(\varphi_1 + \alpha/2) + i \cos(\varphi_1 + \alpha/2)] \\ &\quad - \bar{M}_y [\cos(\varphi_2 + \beta/2) + i \sin(\varphi_2 + \beta/2)], \end{aligned} \quad (29)$$

with $\bar{M}_{x/y} = \mu_B \eta_{m_F}^{m_F} M_{x/y} / 2$.

We consider that the $\lambda/4$ wave plate is placed in the front of both retro-reflected mirrors which corresponds to the extra relative phase difference between two orthogonal polarization $\alpha = \beta = \pi$. For the setting with $(\varphi_1, \varphi_2) = (-\pi/2, 0)$ as shown in Fig. 4(a1), in which the polarization of the Raman laser L_1 along x is chosen as circular while L_2 along y as linear at a $\pi/4$ angle to the vertical direction, $\Omega = i(\bar{M}_x - \bar{M}_y)$ and $\mathbf{\Omega} \cdot \hat{\sigma} = -\hat{\sigma}_z \delta/2 + (\bar{M}_x - \bar{M}_y) \hat{\sigma}_y = -\hat{\sigma}_z \delta/2 - \frac{\Omega_0}{2} \sin[k_R(x-y)] \hat{\sigma}_y$, which corresponds to 1D Raman lattice in the $\hat{x}-\hat{y}$ direction. We can see that 1D Raman lattice in the $\hat{x}-\hat{y}$ direction appears in the absorption images for the momentum-resolved Raman spectroscopy as shown in Fig. 4(a2). When B_0 is reversed to the $-z$ direction that corresponds to the setting with $(\varphi_1, \varphi_2) = (\pi/2, 0)$ as shown in Fig. 4(b1), $\Omega = -i(\bar{M}_x + \bar{M}_y)$ and $\mathbf{\Omega} \cdot \hat{\sigma} = -\hat{\sigma}_z \delta/2 - (\bar{M}_x + \bar{M}_y) \hat{\sigma}_y = -\hat{\sigma}_z \delta/2 + \frac{\Omega_0}{2} \sin[k_R(x+y)] \hat{\sigma}_y$, which corresponds to 1D Raman lattice in the $\hat{x}+\hat{y}$ direction as shown in Fig. 4(b2). Therefore, this case corresponds to the chiral 2D Raman coupling for SOC, in which two orthogonal 1D Raman lattices appear for the positive and negative directions of the magnetic quantization axis respectively.

When we consider the setting with $(\varphi_1, \varphi_2) = (0, 0)$ as shown in Fig. 4(c1) and (d1), in which the polarization of the Raman laser L_1 and L_2 is linear at the $\pm\pi/4$ angle to the vertical direction respectively, $\Omega = \bar{M}_x - i\bar{M}_y$ and $\mathbf{\Omega} \cdot \hat{\sigma} = -\hat{\sigma}_z \delta/2 + \bar{M}_x \hat{\sigma}_x - \bar{M}_y \hat{\sigma}_y$, which corresponds to 2D Raman lattice in the $\hat{x}+\hat{y}$ and $\hat{x}-\hat{y}$ direction. We can see that the 2D Raman lattice in the $\hat{x}+\hat{y}$ and $\hat{x}-\hat{y}$ direction appears in the absorption images for the momentum-resolved Raman spectroscopy as shown in Fig. 4(c2). When B_0 is reversed to the $-z$ direction, $\Omega = \bar{M}_x + i\bar{M}_y$ and $\mathbf{\Omega} \cdot \hat{\sigma} = -\hat{\sigma}_z \delta/2 + \bar{M}_x \hat{\sigma}_x + \bar{M}_y \hat{\sigma}_y$, which corresponds to the similar 2D Raman lattice in the $\hat{x}+\hat{y}$ and $\hat{x}-\hat{y}$ direction as shown in Fig. 4(d2). Therefore, this case corresponds to the non-chiral 2D Raman coupling for SOC, in which the same 2D Raman lattice appears for the positive and negative directions of the magnetic quantization axis respectively. Here, we would like to mention that this case corresponds 2D SOC based on the optical Raman lattice scheme for studying the topological energy band [55, 56].

Furthermore, consider the Raman transition $\delta m_F = 0$ between two hyperfine Zeeman states $|F = 7/2, m_F = 1/2\rangle \equiv |\uparrow\rangle$ and $|F = 9/2, m_F = 1/2\rangle \equiv |\downarrow\rangle$. For this nonchiral transition, only the component of $\hat{\mathbf{e}}_z$ of the effective AC magnetic field $\mathbf{B}_{AC}^{\text{eff}}$ (Eq. (24)) parallel to the static bias field \mathbf{B}_0 can drive transition $\delta m_F = 0$ and the components of $\hat{\mathbf{e}}_x$ and $\hat{\mathbf{e}}_y$ perpendicular to the static bias field \mathbf{B}_0 are neglected. We can see that the same 2D Raman lattice in the $\hat{x}+\hat{y}$ and $\hat{x}-\hat{y}$ direction appears in the absorption images for the momentum-resolved Raman spectroscopy in the positive and negative directions of the magnetic quantization axis respectively, as shown

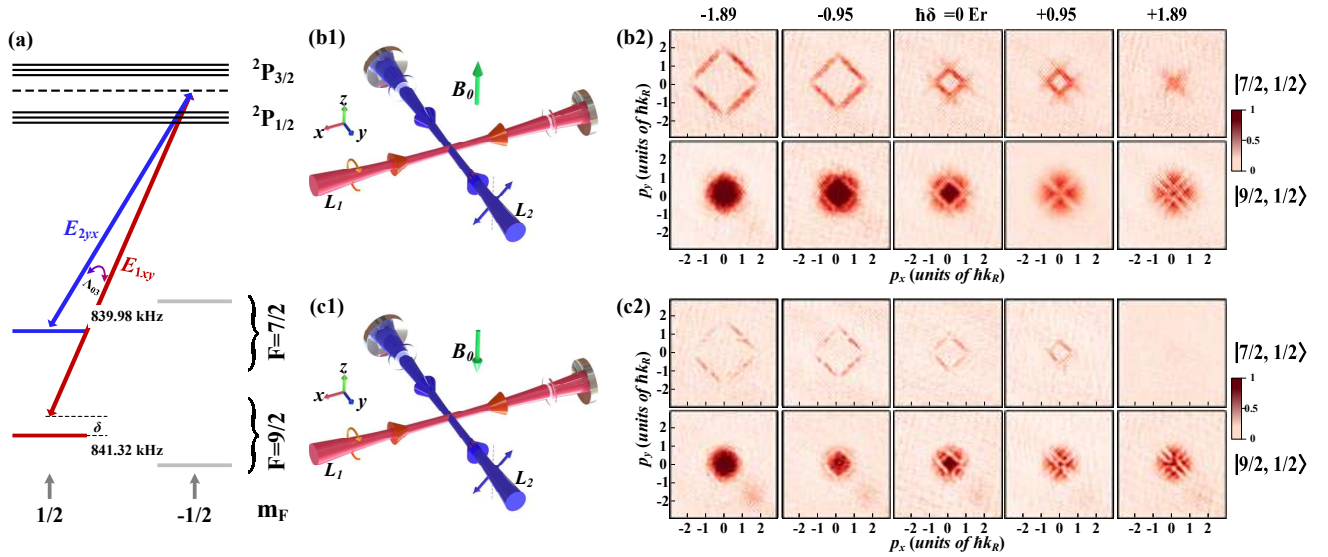


FIG. 5. (Color online). **Raman spectroscopy of 2D Raman coupling for SOC in an optical square Raman lattice for $\delta m_F=0$.** (a) Two Raman lasers drive the nonchiral Raman transition $\delta m_F=0$ between two hyperfine spin states $|F=7/2, m_F=1/2\rangle$ and $|F=9/2, m_F=1/2\rangle$. (b1) and (c1) The polarization of l_L along x is circular while the Raman laser L_2 along y is linear at a $\pi/4$ angle to the vertical direction. The external magnetic field B_0 is along the $+z$ (b1) and $-z$ direction (c1). (b2) and (c2) The absorption images of two hyperfine spin states after 12 ms TOF for different Raman frequency detuning δ .

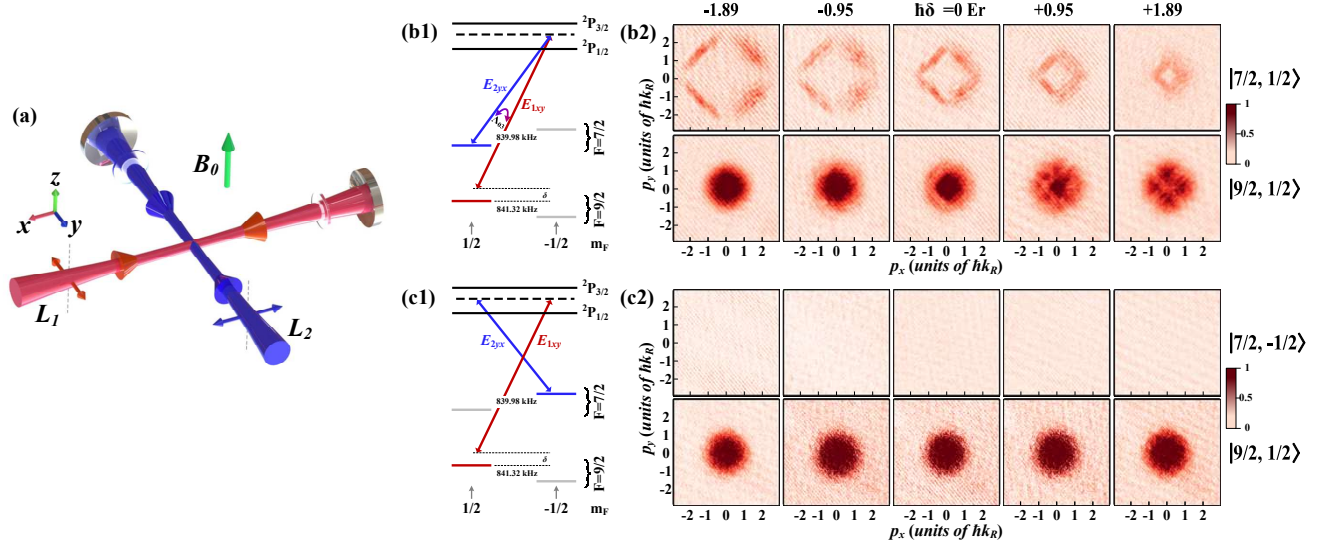


FIG. 6. (Color online). **Raman spectroscopy of 2D Raman coupling for SOC in an optical square Raman lattice comparing $\delta m_F=0$ and ± 1 with the horizontally linear polarisation.** (a) The polarization of Raman laser L_1 along x and L_2 along y all have the horizontally linear polarisation to generate square lattice and Raman coupling respectively. The external magnetic field B_0 is along the $+z$. (b1) and (c1) Two Raman lasers drive the Raman transition $\delta m_F=0$ ($|9/2, 1/2\rangle \rightarrow |7/2, 1/2\rangle$) and $\delta m_F=\pm 1$ ($|9/2, 1/2\rangle \rightarrow |7/2, -1/2\rangle$), respectively. (b2) and (c2) The absorption images of two hyperfine spin states after 12 ms TOF for different Raman frequency detuning δ .

in Fig. 5(a). Therefore, this case corresponds to the nonchiral 2D Raman coupling for SOC. Theoretically, the atomic absorption images from Fig. 4(c2) and (d2), as well as Fig. 5(b2) and (c2) should display exactly the same pattern. However, there are many factors to cause some residual difference of the atomic response in the

realistic experiment. For example, when the magnetic field flips from the $+z$ direction to the $-z$ direction, it is not possible to ensure a perfect 180° flip, which leads to a deviation of the effective AC magnetic field relative to the bias magnetic field. Moreover, the fluctuation of atom number and Raman laser intensity can also cause

the difference of the momentum-resolved Raman spectroscopy.

Finally, consider the Raman transition $\delta m_F=0, \pm 1$ based on two same polarization in x-y plane of Raman lasers as shown in Fig. 6(a), which drive the Raman transition $\delta m_F=0$ ($|9/2, 1/2\rangle \rightarrow |7/2, 1/2\rangle$) and $\delta m_F=\pm 1$ ($|9/2, 1/2\rangle \rightarrow |7/2, -1/2\rangle$), respectively. For this nonchiral Raman transition $\delta m_F=0$ as shown in Fig. 6(b), the component of $\hat{\mathbf{e}}_z$ for the effective AC magnetic field \mathbf{B}_{AC}^{eff} (Eq. (24)) parallel to the static bias field \mathbf{B}_0 , which is same to the case in Fig. 5(a). However, for the transition $\delta m_F=\pm 1$, there is no Raman coupling as shown in Fig. 6(c), since the only component of $\hat{\mathbf{e}}_z$ for AC magnetic field \mathbf{B}_{AC}^{eff} parallel to the static bias field \mathbf{B}_0 can not drive transition $\delta m_F = \pm 1$ to induce disappearance of Raman coupling.

In conclusion, we present the intuitive picture of the chirality of spin motion in a static and AC magnetic field by the Bloch sphere to better understand the physics of the non-chiral and chiral Raman coupling for SOC. We study the chiral Raman coupling created by the chiral light-atom interaction, in which a circularly polarized AC magnetic field generated by two Raman lasers interacts with the chiral transition $\delta m_F=\pm 1$ between two Zeeman spin states. The chirality of Raman coupling for SOC is demonstrated by setting different laser polarization configurations under the different two-photon transition rules. 1D and 2D chiral Raman coupling for SOC are investigated experimentally in detail. This work provides a new system for understanding chiral physics and investigating the states of matter with chirality.

This research is supported by National Key Research and Development Program of China (Grants No. 2022YFA1404101, and No. 2021YFA1401700), Innovation Program for Quantum Science and Technology (Grants No. 2021ZD0302003), National Natural Science Foundation of China (Grants No. 12034011, No. U23A6004, No. 12474266, No. 12474252, No. 12374245, No. 12322409, and No. 92065108), and the Fund for Shanxi 1331 Project Key Subjects Construction.

* Corresponding author email: huanglh06@sxu.edu.cn;

† Corresponding author email: jzhang74@sxu.edu.cn

- [1] M. Yoon, R. Srirambalaji, and K. Kim, Homochiral metal-organic frameworks for asymmetric heterogeneous catalysis, *Chem. Rev.* **112**, 1196 (2012).
- [2] B. A. McGuire, P. B. Carroll, R. A. Loomis, I. A. Finneran, P. R. Jewell, A. J. Remijan, and G. A. Blake, Discovery of the interstellar chiral molecule propylene oxide ($\text{CH}_3\text{CHCH}_2\text{O}$), *Science* **352**, 1449 (2016).
- [3] Y. Chen, H. Deng, X. Sha, W. Chen, R. Wang, Y.-H. Chen, D. Wu, J. Chu, Y. S. Kivshar, S. Xiao, and C.-W. Qiu, Observation of intrinsic chiral bound states in the continuum, *Nature* **613**, 474 (2023).
- [4] C. Kallin and J. Berlinsky, Chiral Superconductors, *Rep. Prog. Phys.* **79**, 054502 (2016).
- [5] K. Shibata, X. Z. Yu, T. Hara, D. Morikawa, N. Kanazawa, K. Kimoto, S. Ishiwata, Y. Matsui, and Y. Tokura, Towards Control of the Size and Helicity of Skyrmions in Helimagnetic Alloys by Spin-Orbit Coupling, *Nature Nanotech* **8**, 723 (2013).
- [6] G. Chen, T. Ma, A. T. N'Diaye, H. Kwon, C. Won, Y. Wu, and A. K. Schmid, Tailoring the chirality of magnetic domain walls by interface engineering, *Nat Commun* **4**, 2671 (2013).
- [7] S. Emori, U. Bauer, S.-M. Ahn, E. Martinez, and G. S. D. Beach, Current-Driven Dynamics of Chiral Ferromagnetic Domain Walls, *Nature Mater* **12**, 611 (2013).
- [8] K.-S. Ryu, L. Thomas, S.-H. Yang, and S. Parkin, Chiral Spin Torque at Magnetic Domain Walls, *Nature Nanotech* **8**, 527 (2013).
- [9] S.-H. Yang, R. Naaman, Y. Paltiel, and S. S. P. Parkin, Chiral Spintronics, *Nat. Rev. Phys.* **3**, 328 (2021).
- [10] M. Atala, M. Aidelsburger, M. Lohse, J. T. Barreiro, B. Paredes, and I. Bloch, Observation of Chiral Currents with Ultracold Atoms in Bosonic Ladders, *Nature Phys* **10**, 588 (2014).
- [11] H. Weng, C. Fang, Z. Fang, B. A. Bernevig, and X. Dai, Weyl Semimetal Phase in Noncentrosymmetric Transition-Metal Monophosphides, *Phys. Rev. X* **5**, 011029 (2015).
- [12] S.-H. Gong, F. Alpeggiani, B. Sciacca, E. C. Garnett, and L. Kuipers, Nanoscale Chiral Valley-Photon Interface through Optical Spin-Orbit Coupling, *Science* **359**, 443 (2018).
- [13] P. Lodahl, S. Mahmoodian, S. Stobbe, A. Rauschenbeutel, P. Schneeweiss, J. Volz, H. Pichler, and P. Zoller, Chiral Quantum Optics, *Nature* **541**, 473 (2017).
- [14] A. Lininger, G. Palermo, A. Guglielmelli, G. Nicoletta, M. Goel, M. Hinczewski, and G. Strangi, Chirality in Light-Matter Interaction, *Advanced Materials* **35**, 2107325 (2023).
- [15] D. Ayuso, O. Neufeld, A. F. Ordonez, P. Decleva, G. Lerner, O. Cohen, M. Ivanov, and O. Smirnova, Synthetic chiral light for efficient control of chiral light-matter interaction, *Nat. Photonics* **13**, 866 (2019).
- [16] S. Yoo and Q.-H. Park, Chiral light-matter interaction in optical resonators, *Phys. Rev. Lett.* **114**, 203003 (2015).
- [17] Y.-J. Lin, K. Jiménez-García, and I. B. Spielman, Spin-orbit-coupled Bose-Einstein condensates, *Nature* **471**, 83 (2011).
- [18] P. Wang, Z. Yu, Z. Fu, J. Miao, L. Huang, S. Chai, H. Zhai, and J. Zhang, Spin-Orbit Coupled Degenerate Fermi Gases, *Phys. Rev. Lett.* **109**, 095301 (2012).
- [19] L. W. Cheuk, A. T. Sommer, Z. Hadzibabic, T. Yefsah, W. S. Bakr, and M. W. Zwierlein, Spin-Injection Spectroscopy of a Spin-Orbit Coupled Fermi Gas, *Phys. Rev. Lett.* **109**, 095302 (2012).
- [20] L. Huang, Z. Meng, P. Wang, P. Peng, S. L. Zhang, L. Chen, D. Li, Q. Zhou, and J. Zhang, Experimental realization of two-dimensional synthetic spin-orbit coupling in ultracold Fermi gases, *Nat. Phys.* **12**, 540 (2016).
- [21] N. Q. Burdick, Y. Tang, and B. L. Lev, Long-lived spin-orbit-coupled degenerate dipolar fermi gas, *Phys. Rev. X* **6**, 031022 (2016).
- [22] Z. Wu, L. Zhang, W. Sun, X.-T. Xu, B.-Z. Wang, S.-C. Ji, Y. Deng, S. Chen, X.-J. Liu, and J.-W. Pan, Realization of two-dimensional spin-orbit coupling for Bose-Einstein

- condensates, *Science* **354**, 83 (2016).
- [23] M. L. Wall, A. P. Koller, S. Li, X. Zhang, N. R. Cooper, J. Ye, and A. M. Rey, Synthetic Spin-Orbit Coupling in an Optical Lattice Clock, *Phys. Rev. Lett.* **116**, 035301 (2016).
- [24] L. F. Livi, G. Cappellini, M. Diem, L. Franchi, C. Clivati, M. Frittelli, F. Levi, D. Calonico, J. Catani, M. Inguscio, and L. Fallani, Synthetic Dimensions and Spin-Orbit Coupling with an Optical Clock Transition, *Phys. Rev. Lett.* **117**, 220401 (2016).
- [25] H.-R. Chen, K.-Y. Lin, P.-K. Chen, N.-C. Chiu, J.-B. Wang, C.-A. Chen, P. Huang, S.-K. Yip, Y. Kawaguchi, and Y.-J. Lin, Spin-Orbital-Angular-Momentum Coupled Bose-Einstein Condensates, *Phys. Rev. Lett.* **121**, 113204 (2018).
- [26] Z.-Y. Wang, X.-C. Cheng, B.-Z. Wang, J.-Y. Zhang, Y.-H. Lu, C.-R. Yi, S. Niu, Y. Deng, X.-J. Liu, S. Chen, and J.-W. Pan, Realization of an Ideal Weyl Semimetal Band in a Quantum Gas with 3D Spin-Orbit Coupling, *Science* **372**, 271 (2021).
- [27] H. Zhai, SPIN-ORBIT COUPLED QUANTUM GASES, *Int. J. Mod. Phys. B* **26**, 1230001 (2012).
- [28] X. Zhou, Y. Li, Z. Cai, and C. Wu, Unconventional states of bosons with the synthetic spin-orbit coupling, *J. Phys. B: At. Mol. Opt. Phys.* **46**, 134001 (2013).
- [29] P.-J. Wang and J. Zhang, Spin-Orbit Coupling in Bose-Einstein Condensate and Degenerate Fermi Gases, *Front. Phys.* **9**, 598 (2014).
- [30] J. Dalibard, F. Gerbier, G. Juzeliūnas, and P. Öhberg, Colloquium: Artificial gauge potentials for neutral atoms, *Rev. Mod. Phys.* **83**, 1523 (2011).
- [31] X.-Q. Xu and J. H. Han, Emergence of Chiral Magnetism in Spinor Bose-Einstein Condensates with Rashba Coupling, *Phys. Rev. Lett.* **108**, 185301 (2012).
- [32] V. Galitski and I. B. Spielman, Spin-orbit coupling in quantum gases, *Nature* **494**, 49 (2013).
- [33] N. Goldman, G. Juzeliūnas, P. Öhberg, and I. B. Spielman, Light-Induced Gauge Fields for Ultracold Atoms, *Rep. Prog. Phys.* **77**, 126401 (2014).
- [34] H. Zhai, Degenerate quantum gases with spin-orbit coupling: A review, *Rep. Prog. Phys.* **78**, 026001 (2015).
- [35] Z. Meng, L. Huang, P. Peng, D. Li, L. Chen, Y. Xu, C. Zhang, P. Wang, and J. Zhang, Experimental Observation of a Topological Band Gap Opening in Ultracold Fermi Gases with Two-Dimensional Spin-Orbit Coupling, *Phys. Rev. Lett.* **117**, 253304 (2016).
- [36] J. Li, W. Huang, B. Shteynas, S. Burchesky, F. Ç. Top, E. Su, J. Lee, A. O. Jamison, and W. Ketterle, Spin-Orbit Coupling and Spin Textures in Optical Superlattices, *Phys. Rev. Lett.* **117**, 185301 (2016).
- [37] S.-S. Zhang, W.-M. Liu, and H. Pu, Itinerant chiral ferromagnetism in a trapped Rashba spin-orbit-coupled Fermi gas, *Phys. Rev. A* **93**, 043602 (2016).
- [38] C. Hamner, C. Qu, Y. Zhang, J. Chang, M. Gong, C. Zhang, and P. Engels, Dicke-type phase transition in a spin-orbit-coupled Bose-Einstein condensate, *Nat. Commun.* **5**, 4023 (2014).
- [39] J.-R. Li, J. Lee, W. Huang, S. Burchesky, B. Shteynas, F. Ç. Top, A. O. Jamison, and W. Ketterle, A stripe phase with supersolid properties in spin-orbit-coupled Bose-Einstein condensates, *Nature* **543**, 91 (2017).
- [40] W. Han, X.-F. Zhang, D.-S. Wang, H.-F. Jiang, W. Zhang, and S.-G. Zhang, Chiral Supersolid in Spin-Orbit-Coupled Bose Gases with Soft-Core Long-Range Interactions, *Phys. Rev. Lett.* **121**, 030404 (2018).
- [41] L. Huang, P. Peng, D. Li, Z. Meng, L. Chen, C. Qu, P. Wang, C. Zhang, and J. Zhang, Observation of Floquet bands in driven spin-orbit-coupled fermi gases, *Phys. Rev. A* **98**, 013615 (2018).
- [42] C.-H. Li, C. Qu, R. J. Niffenegger, S.-J. Wang, M. He, D. B. Blasing, A. J. Olson, C. H. Greene, Y. Lyanda-Geller, Q. Zhou, C. Zhang, and Y. P. Chen, Spin current generation and relaxation in a quenched spin-orbit-coupled Bose-Einstein condensate, *Nat. Commun.* **10**, 375 (2019).
- [43] A. Valdés-Curiel, D. Trypogeorgos, Q.-Y. Liang, R. P. Anderson, and I. B. Spielman, Topological features without a lattice in Rashba spin-orbit coupled atoms, *Nat Commun* **12**, 593 (2021).
- [44] I. H. Deutsch and P. S. Jessen, Quantum-state control in optical lattices, *Phys. Rev. A* **57**, 1972 (1998).
- [45] G. Juzeliūnas and I. B. Spielman, Flux lattices reformulated, *New J. Phys.* **14**, 123022 (2012).
- [46] I. B. Spielman, Raman processes and effective gauge potentials, *Phys. Rev. A* **79**, 063613 (2009).
- [47] T.-L. Ho and S. Zhang, Bose-Einstein condensates with spin-orbit interaction, *Phys. Rev. Lett.* **107**, 150403 (2011).
- [48] B. M. Anderson, G. Juzeliūnas, V. M. Galitski, and I. B. Spielman, Synthetic 3D Spin-Orbit Coupling, *Phys. Rev. Lett.* **108**, 235301 (2012).
- [49] Y. Li, G. I. Martone, L. P. Pitaevskii, and S. Stringari, Superstripes and the Excitation Spectrum of a Spin-Orbit-Coupled Bose-Einstein Condensate, *Phys. Rev. Lett.* **110**, 235302 (2013).
- [50] S. Chai, P. Wang, Z. Fu, L. Huang, and J. Zhang, The Design of a dipole traps for Bose-Einstein Condensate and Degenerate Fermi Gas, *Acta Sin. Quantum Opt.* **18**, 171 (2012).
- [51] J. Miao, G. Bian, B. Shan, L. Chen, Z. Meng, P. Wang, L. Huang, and J. Zhang, Achieving ultracold Bose-Fermi mixture of ^{87}Rb and ^{40}K with dual dark magnetic-optical-trap, *Chin. Phys. B* **31**, 080306 (2022).
- [52] P. Ding, B. Shan, Y. Zhao, Y. Yang, L. Chen, Z. Meng, P. Wang, L. Huang, and J. Zhang, Optimal preparation of Bose and Fermi atomic gas mixtures for ^{87}Rb and ^{40}K in a crossed optical dipole trap, *Chin. Phys. B* **33**, 063402 (2024).
- [53] R. Trubko, M. D. Gregoire, W. F. Holmgren, and A. D. Cronin, Potassium tune-out-wavelength measurement using atom interferometry and a multipass optical cavity, *Phys. Rev. A* **95**, 052507 (2017).
- [54] G. Bian, L. Huang, D. Li, Z. Meng, L. Chen, P. Wang, and J. Zhang, Realization of space-dependent interactions by an optically controlled magnetic p -wave Feshbach resonance in degenerate Fermi gases, *Phys. Rev. A* **106**, 023322 (2022).
- [55] W. Sun, C.-R. Yi, B.-Z. Wang, W.-W. Zhang, B. C. Sanders, X.-T. Xu, Z.-Y. Wang, J. Schmiedmayer, Y. Deng, X.-J. Liu, S. Chen, and J.-W. Pan, Uncover Topology by Quantum Quench Dynamics, *Phys. Rev. Lett.* **121**, 250403 (2018).
- [56] C.-R. Yi, L. Zhang, L. Zhang, R.-H. Jiao, X.-C. Cheng, Z.-Y. Wang, X.-T. Xu, W. Sun, X.-J. Liu, S. Chen, and J.-W. Pan, Observing topological charges and dynamical bulk-surface correspondence with ultracold atoms, *Phys. Rev. Lett.* **123**, 190603 (2019).